Check for updates

ADVANCED FUNCTIONAL MATERIALS
www.afm-journal.de

Seamlessly Integrated, High-Output and Robust Triboelectric Nanoyarns: Continuously Electrospun Core-Sheath Architectures for Multimodal Sensing Platforms

Yiqun Chen, Jinrong Huang, Zixuan Liu, Yi Zou, Jianwen Chen, Zunfeng Liu,* and Yutian Zhu**

Textile-based triboelectric nanogenerators (TENGs) have emerged as a transformative technology for self-powered wearable electronics. However, current textile-based TENGs predominantly employ multilayer architectures that introduce critical trade-offs: elevated mechanical rigidity, compromised air permeability, and interfacial instability. More fundamentally, their 2D geometry impedes textile-process integration and restricts dynamic biomechanical compatibility. To overcome these issues, a coaxial nanofiber yarn-based single-electrode TENG through a scalable one-step electrospinning that eliminates multilayer assembly via multiscale engineered core-sheath integration is developed. This approach achieves performance integration across multiple scales: through incorporating $Cs_3Bi_2Cl_9$ into poly(vinylidene fluoride-co-trifluoroethylene) (PVDF-TrFE) to enhance molecular-scale β-phase and dielectric properties, optimizing surface roughness at the micro/nano-scale, and forming a macroscale core-sheath structure with a triboelectric PVDF-TrFE/$Cs_3Bi_2Cl_9$ sheath. The resulting TENG demonstrates enhanced output performance and operational stability, thus enabling multifunctional applications including interactive guzheng digitization interfaces, textile classification with 95.83% accuracy, and self-powered Morse communication systems. When woven into a 2D fabric, this TENG achieves high-pressure sensitivity (3.64 V kPa^{-1}), broad detection range (up to 50 kPa), extreme durability (>50 000 cycles), as well as inherent breathability, biocompatibility, and industrial washability. This work establishes a high-performance yarn-based TENG through scalable electrospinning, demonstrating practical applications in smart musical instruments and machine learning-enhanced fabric identification systems.

1. Introduction

Triboelectric nanogenerators (TENGs) have attracted significant attention in the fields of energy harvesting and intelligent sensing in recent years, owing to their unique ability to convert ambient mechanical energy into electricity through contact electrification and electrostatic induction.[1–5] With key advantages such as broad material choices, excellent eco-compatibility, and efficient energy harvesting capability, TENGs are increasingly recognized as a key enabling technology for emerging self-powered wearable electronics and distributed IoT applications. Among various architectures, textile-based TENGs stand out due to their intrinsic compatibility with clothing systems, offering unparalleled flexibility, breathability, and seamless integration into everyday textiles.[6–10]

The triboelectric performance of textile-based TENGs is fundamentally determined by two critical factors: the intrinsic material characteristics (including electron affinity, dielectric polarization, and permittivity) and the strategically designed surface morphology that directly modulates the effective contact area.[11–13] To boost the electrical output of textile-based TENG systems, researchers have

Y. Chen, J. Huang, Z. Liu, Y. Zou, J. Chen, Y. Zhu
Key Laboratory of Organosilicon Chemistry and Material Technology, Ministry of Education, Zhejiang Key Laboratory of Organosilicon Material Technology, College of Material, Chemistry and Chemical Engineering
Hangzhou Normal University
Hangzhou, Zhejiang 311121, P. R. China
E-mail: jwchen@hznu.edu.cn; ytzhu@hznu.edu.cn

Z. Liu
State Key Laboratory of Medicinal Chemical Biology, Key Laboratory of Functional Polymer Materials, Tianjin Key Laboratory of Functional Polymer Materials, Smart Sensing Interdisciplinary Science Center, College of Chemistry
Nankai University
Tianjin 300350, P. R. China
E-mail: liuzunfeng@nankai.edu.cn

The ORCID identification number(s) for the author(s) of this article can be found under https://doi.org/10.1002/adfm.202523166

DOI: 10.1002/adfm.202523166

 © 2025 Wiley-VCH GmbH

systematically optimized both material compositions and surface engineering methodologies through various techniques. Among diverse triboelectric materials, poly(vinylidene fluoride) (PVDF) and its copolymers, particularly poly(vinylidene fluoride-co-trifluoroethylene) (PVDF-TrFE) and poly(vinylidene fluoride-co-hexafluoropropylene) (PVDF-HFP), are widely recognized as high-performance triboelectrically negative materials.[14–17] The strong electron affinity inherent to fluorine-rich molecular structures enhances both charge density generation and retention in textile-based TENGs. To maximize their triboelectric potential, strategic material engineering approaches involving functional filler incorporation and advanced processing optimization have been developed.[18–22] Compared to conventional functional fillers (e.g., graphene,[23,24] molybdenum disulfide,[25] and MXene[26]), perovskites exhibit unique multifunctional superiority in TENG systems by synergistically combining their high intrinsic dielectric permittivity, charge-trapping capability, and β-phase nucleation effects. The inherent ionic defects and polarized crystal structures of perovskites not only create deep charge-trapping sites to stabilize interfacial charges but also induce preferential alignment of PVDF dipoles, simultaneously amplifying dielectric polarization via their ferroelectrically active lattices.[27,28]

Among various fabrication processes for textile-based TENGs (such as wet spinning, electrospinning, coating, and film encapsulation), electrospinning stands out by synergistically elevating the triboelectric performance of PVDF composites through dual optimization: enhancing β-phase crystallinity while engineering high-surface-area fibrous architectures, thereby amplifying dielectric polarization and interfacial charge generation.[29–31] Current electrospun textile-based TENGs predominantly employ a multilayer sandwiched architecture, where triboelectrically opposing fabric layers are encapsulated between conductive electrodes. While effective for charge generation, this configuration introduces critical structural trade-offs: the accumulated layers not only elevate mechanical rigidity but also compromise air permeability and operational stability. More critically, the inherent geometric characteristics of this configuration hinder seamless integration during textile weaving processes and restrict dynamic compatibility with human biomechanics. These limitations directly degrade essential textile functionalities, ultimately challenging their practical implementation in wearable systems.

To address these limitations, we proposed a single-electrode coaxial nanofiber yarn TENG (CNY-SE-TENG) fabricated via a scalable one-step electrospinning. The TENG architecture integrated a silver-plated nylon conductive core with a PVDF-TrFE composite shell incorporating lead-free $Cs_3Bi_2Cl_9$ perovskite nanocrystals. Through this multiscale structure engineering strategy, including molecular-scale enhancement of β-phase crystallinity and dielectric properties in PVDF-TrFE via $Cs_3Bi_2Cl_9$ incorporating, micro/nano-scale surface morphology optimization, and macroscale core-shell structural design, the TENG achieved simultaneous improvement in both output performance and operational stability. The CNY-SE-TENG's integration into textile architectures demonstrated inherent self-powered sensing capabilities, exhibiting high sensitivity, robust durability and superior wearability, which validate its practical applicability for next-generation self-powered wearable devices.

2. Discussion

2.1. Structure Design and Material Characterization

The PVDF-TrFE/$Cs_3Bi_2Cl_9$ CNYs for TENG assembly were fabricated through coaxial conjugated electrospinning, where PVDF-TrFE/$Cs_3Bi_2Cl_9$ nanofibers were deposited onto silver-plated nylon yarn (**Figure 1a**). In this process, oppositely charged electrospinning jets mutually attracted under the electric field and co-deposited onto a grounded trumpet-shaped collector. Simultaneously, the silver-plated nylon yarn advanced axially through the collector's center via take-up roller traction. The collector's rotation enabled uniform nanofiber wrapping around the yarn, producing the final PVDF-TrFE/$Cs_3Bi_2Cl_9$ CNYs. The resulting batch-produced CNYs (Figure 1b) withstand axial tensile loads up to 500 g while maintaining structural integrity, and exhibit sufficient flexibility for knitting/weaving applications, demonstrating enhanced processability for post-textile manufacturing.

Lead-free $Cs_3Bi_2Cl_9$ perovskite microcrystals were synthesized as functional additives to enhance the triboelectric performance of PVDF-TrFE. Structural characterization through XRD revealed a well-defined orthorhombic phase, with characteristic peaks at 19.7°, 23.4°, 30.7°, 33.3°, 36.4°, 41.1°, 43.7°, 47.8°, and 53.8° corresponding to the (113), (130), (223), (224), (117), (330), (227), (260), and (318) crystallographic planes,[32,33] respectively (Figure 1c). The diffraction pattern exhibited precise alignment with the reference JCPDS 70-0990, confirming phase purity and successful crystallization. Complementary morphological analysis via FESEM demonstrated micron-scale crystallites with an average particle size of 1.0 µm (Figure 1d). EDS elemental mapping confirmed homogeneous spatial distribution of Cs, Bi, and Cl elements.

To investigate the interfacial interaction mechanism between PVDF-TrFE and $Cs_3Bi_2Cl_9$ (Figure 1e), we performed XPS characterization on PVDF-TrFE, $Cs_3Bi_2Cl_9$, and the PVDF-TrFE/$Cs_3Bi_2Cl_9$ composite. All spectra were charge-corrected by referencing the adventitious carbon peak (C 1s, 284.8 eV). As shown in Figure S1a (Supporting Information), characteristic peaks corresponding to the CH_2, CHF, and CF_2 groups in PVDF-TrFE were observed at 286.1, 288.2, and 290.6 eV, respectively, in both PVDF-TrFE and the composite.[34] A minor peak attributed to CF_3 terminal groups was also detected at 293.0 eV. In contrast, the $Cs_3Bi_2Cl_9$ sample exhibited only the adventitious carbon signal at 284.8 eV.

Upon the introduction of $Cs_3Bi_2Cl_9$, the F 1s binding energy showed a positive shift of 0.19 eV (Figure 1f), indicating an interaction between PVDF-TrFE and $Cs_3Bi_2Cl_9$.[35] Correspondingly, after incorporating PVDF-TrFE, the binding energies of the Cl 2p orbitals in $Cs_3Bi_2Cl_9$ exhibited a negative shift of 0.31 eV (Figure 1g), while the Bi 4f orbitals also showed a smaller negative shift of 0.16 eV (Figure S1b, Supporting Information). Due to the electron-withdrawing effect of F atoms, the adjacent hydrogen atoms carry a partial positive charge density. Consequently, the all-trans planar zigzag conformation of PVDF in PVDF-TrFE renders it Lewis-acid-like, enabling interaction with the perovskite surface.[36] Combined with the observed red-shift of the asymmetric (ν_{as}) stretching vibration peak of the CH_2 group in FT-IR (from 3020 to 3017 cm^{-1}, Figure 1h), we attribute the negative shifts in the Bi and Cl binding energies to interactions formed

© 2025 Wiley-VCH GmbH

16163028, 0, Downloaded from https://advanced.onlinelibrary.wiley.com/doi/10.1002/adfm.202523166 by Hangzhou Normal University, Wiley Online Library on [20/11/2025]. See the Terms and Conditions (https://onlinelibrary.wiley.com/terms-and-conditions) on Wiley Online Library for rules of use; OA articles are governed by the applicable Creative Commons License

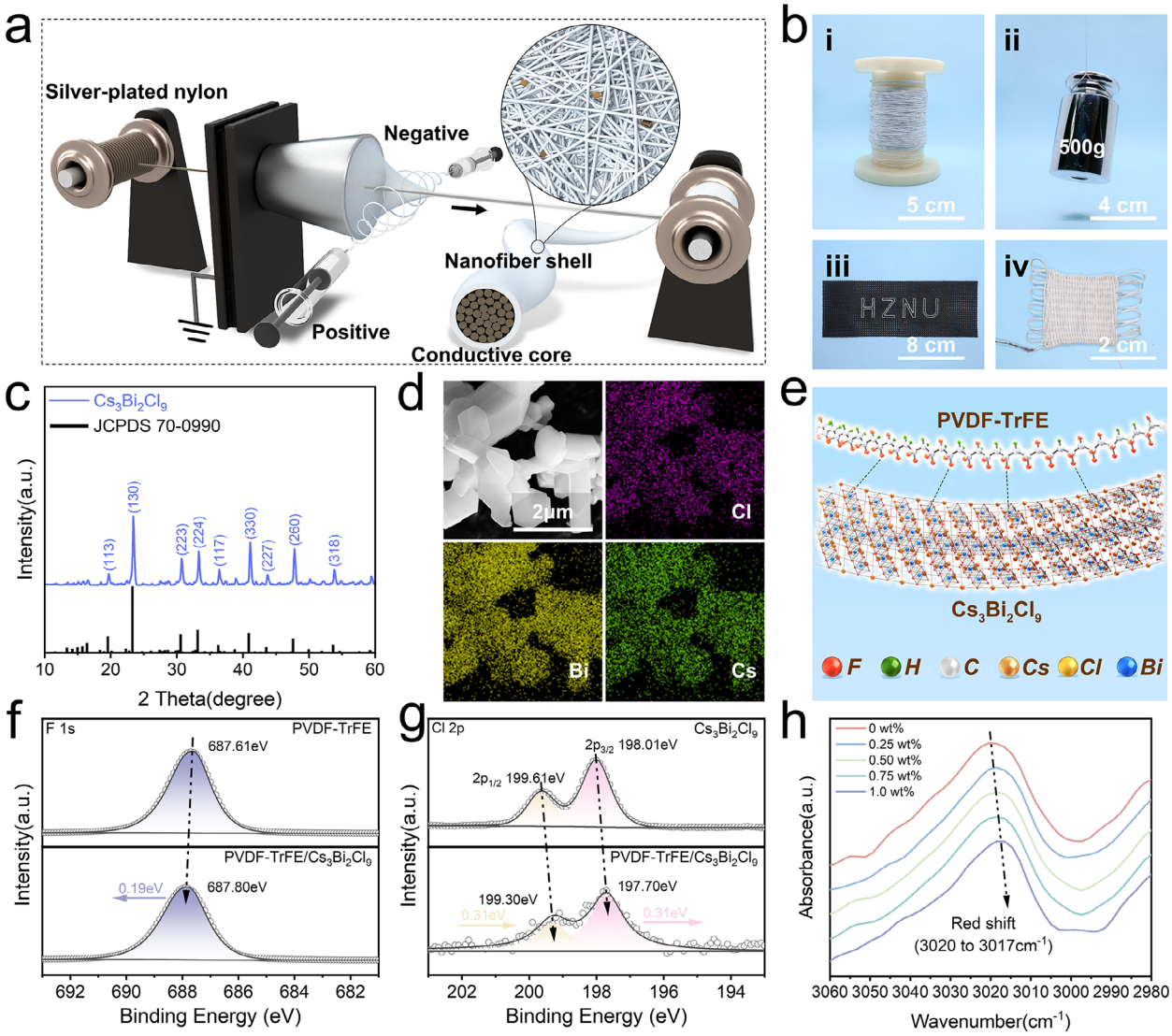

Figure 1. a) Schematic of coaxial conjugated electrospinning process for CNYs. b) Optical photographs of PVDF-TrFE/$Cs_3Bi_2Cl_9$ CNYs: i) a roll of CNYs, ii) supporting a 500 g weight, iii) cross-stitched "HZNU" pattern, iv) woven into twill fabric. c) XRD patterns of $Cs_3Bi_2Cl_9$ microcrystals. d) SEM image of $Cs_3Bi_2Cl_9$ and corresponding elemental maps. e) Schematic illustration of the interaction between $Cs_3Bi_2Cl_9$ and PVDF-TrFE. f) F 1s spectra of pure PVDF-TrFE and PVDF-TrFE /$Cs_3Bi_2Cl_9$ composite, g) Cl 2p spectra of $Cs_3Bi_2Cl_9$ and PVDF-TrFE /$Cs_3Bi_2Cl_9$ composite. h) FT-IR spectra of $\nu_{as}(CH_2)$ for PVDF-TrFE and the PVDF-TrFE/$Cs_3Bi_2Cl_9$ composite.

between the CFH/CH_2 dipoles in PVDF-TrFE and the Cl^- ions in the $[Bi_2Cl_9]^{3-}$ clusters via C-H···Cl ion-dipole interactions.[37,38] In contrast to the trends observed for Cl and Bi, the binding energy of Cs exhibited a positive shift. As shown in Figure S1c (Supporting Information), the binding energy of the Cs 3d orbitals increased by 0.18 eV. We speculate that this may result from electron redistribution induced by the complex interfacial interaction between PVDF-TrFE and $Cs_3Bi_2Cl_9$.

The distinct microstructural evolution in CNYs before and after $Cs_3Bi_2Cl_9$ incorporation was further investigated through SEM analysis (**Figure** 2a–f). The pristine PVDF-TrFE CNYs display yarn diameter of 510 μm (drawing rate of 1.5 rpm, Figure 2a), with surface topography dominated by interconnected nanofibers averaging 750 nm in diameter (Figure 2b). As further shown in Figure S2 (Supporting Information), the yarn diameter decreases with increasing drawing rate. Cross-sectional SEM image and element mapping (Figure 2c) confirm the distinct core-shell architecture of PVDF-TrFE CNYs. The incorporation of perovskite induces progressive nanoscale refinement while preserving the macroscopic yarn architecture's dimensional stability (Figure 2d–f). Surface nanofiber diameters decrease with increasing concentration from 750 to 530 nm as perovskite content rises from 0 wt.% to 1.0 wt.% (Figure 2b,e; Figure S3, Supporting Information). This trend is attributed to $Cs_3Bi_2Cl_9$ incorporation, which markedly enhances solution polarization and consequently intensifies the electrostatic stretching force during electrospinning, ultimately yielding finer fibers.[39] Crucially, $Cs_3Bi_2Cl_9$ nanocrystals preferentially distribute along nanofiber surfaces (Figure 2e), establishing charge-enriched heterointerfaces that enhance triboelectric output.

© 2025 Wiley-VCH GmbH

16163028, 0, Downloaded from https://advanced.onlinelibrary.wiley.com/doi/10.1002/adfm.202523166 by Hangzhou Normal University, Wiley Online Library on [20/11/2025]. See the Terms and Conditions (https://onlinelibrary.wiley.com/terms-and-conditions) on Wiley Online Library for rules of use; OA articles are governed by the applicable Creative Commons License

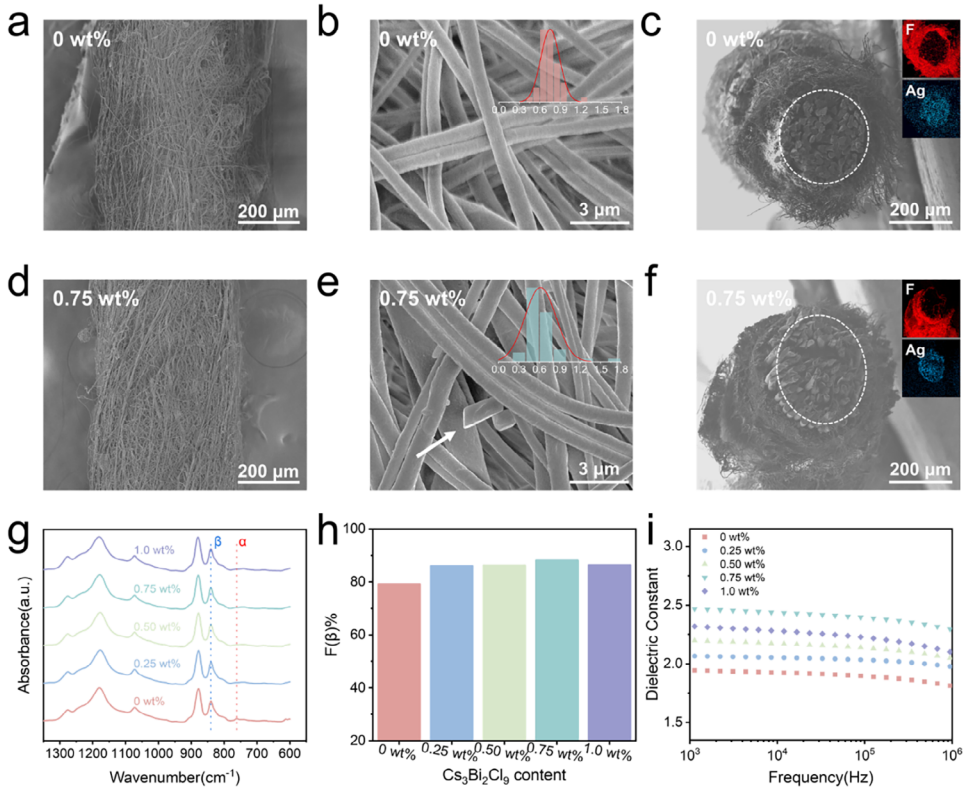

Figure 2. a–c) PVDF-TrFE CNYs (drawing rate: 1.5 rpm): a) low-magnification SEM image, b) high-magnification SEM image, c) cross-sectional SEM image with corresponding EDS elemental maps of F and Ag. d–f) CNYs containing 0.75 wt.% $Cs_3Bi_2Cl_9$ (drawing rate: 1.5 rpm): d) low-magnification SEM image, e) high-magnification SEM image, f) cross-sectional SEM image and EDS maps (F, Ag) of the PVDF-TrFE/$Cs_3Bi_2Cl_9$ yarn. g) FT-IR spectra of PVDF-TrFE/$Cs_3Bi_2Cl_9$ yarns with varying $Cs_3Bi_2Cl_9$ content (0 wt.%–1.0 wt.%). h) Calculated β-phase crystal content of PVDF-TrFE/$Cs_3Bi_2Cl_9$ composites. i) Dielectric constant of PVDF-TrFE/$Cs_3Bi_2Cl_9$ composites with different incorporation contents as a function of frequency.

Beyond yarn morphology, the incorporation of perovskite significantly modulates the polar β-phase content and dielectric properties of PVDF-TrFE yarn, thereby enhancing their triboelectric output performance. The β-phase content of PVDF-TrFE before and after $Cs_3Bi_2Cl_9$ incorporation was analyzed through FTIR (Figure 2g). Characteristic absorption bands at 762 and 841 cm^{-1} were assigned to the nonpolar α-phase and polar β-phase, respectively.[40,41] The relative β-phase content was quantitatively determined using Beer-Lambert law (Equation (1)):

$$F_\beta = \frac{A_\beta}{\left(\frac{K_\beta}{K_\alpha}\right) \cdot A_\alpha + A_\beta} \quad (1)$$

where A_α and A_β represent the absorbance at 762 and 841 cm^{-1}, with corresponding absorption coefficients $K_\alpha = 6.1 \times 10^4$ cm^2 mol^{-1} and $K_\beta = 7.7 \times 10^4$ cm^2 mol^{-1}.[23,42] Remarkably, the incorporation of $Cs_3Bi_2Cl_9$ induced a significant increase in β-phase content through ion-dipole interactions between $Cs_3Bi_2Cl_9$ and PVDF-TrFE, which induced all-trans (TTTT) chain conformation. The β-phase content reaches a maximum value of 88.12% at a perovskite concentration of 0.75 wt.% (Figure 2h).

The dielectric properties of PVDF-TrFE composites have also been significantly enhanced after incorporating $Cs_3Bi_2Cl_9$ through two synergistic mechanisms: by promoting the formation of polar β-phase crystals and through the intrinsic high dielectric constant of the perovskite filler.[43,44] Figure 2i demonstrates that the relative dielectric constant (ϵ') of the composites first increases then decreases with increasing $Cs_3Bi_2Cl_9$ content, reaching a maximum value of 2.46 at 10^3 Hz for the 0.75 wt.% composite (a 27% enhancement compared to the pristine polymer ($\epsilon' \approx 1.94$)). It should be noted that the measured dielectric constants are relatively low, which is primarily attributed to the highly porous structure of the electrospun nanofiber membranes that introduces a significant volume of air, thereby reducing the overall dielectric constant of the composite. This optimal loading concentration likely results from balanced filler dispersion and interfacial polarization effects. Importantly, as revealed by dielectric loss analysis in Figure S4 (Supporting Information), the composite maintains excellent dielectric loss characteristics at appropriate $Cs_3Bi_2Cl_9$ loadings, demonstrating well-optimized dielectric performance.

2.2. Mechanism and Output Performance of the CNY-SE-TENG Device

Figure 3a systematically illustrates the operational principle of the CNY-SE-TENG.[45,46] The system integrates a PVDF-TrFE/$Cs_3Bi_2Cl_9$ nanofiber composite (tribo-negative layer) with

© 2025 Wiley-VCH GmbH

16163028, 0, Downloaded from https://advanced.onlinelibrary.wiley.com/doi/10.1002/adfm.202523166 by Hangzhou Normal University, Wiley Online Library on [20/11/2025]. See the Terms and Conditions (https://onlinelibrary.wiley.com/terms-and-conditions) on Wiley Online Library for rules of use; OA articles are governed by the applicable Creative Commons License

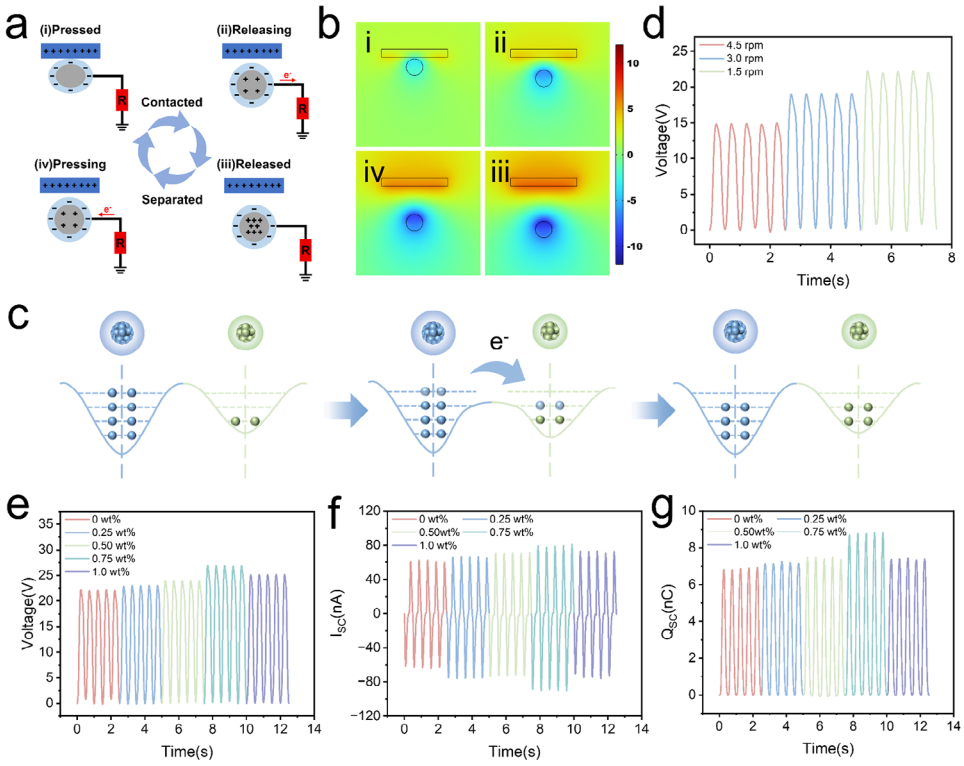

Figure 3. a) Working principle of the CNY-SE-TENG. b) Simulated potential distribution of the CNY-SE-TENG. c) Atomic-scale electron cloud potential well model describing electron transfer in CNY-SE-TENG. d) Open-circuit voltage of the CNY-SE-TENG assembled from yarns electrospun at different drawing rates. e) Output voltage, f) short-circuit current, and g) transferred charge under short-circuit conditions of the CNY-SE-TENG with varying $Cs_3Bi_2Cl_9$ loading.

silver-nylon yarn electrodes, operating in single-electrode mode. During cyclic contact-separation motions, the coupled effects of triboelectric charge transfer and electrostatic induction generate alternating current output through four distinct phases: initial contact induces interfacial charge transfer and surface charging (Figure 3a(i)); subsequent separation disrupts electrostatic balance and drives electron flow through the external circuit (Figure 3a(ii)); complete separation establishes transient equilibrium (Figure 3a(iii)); and renewed contact initiates reverse charge transfer to complete the periodic electrical generation cycle (Figure 3a(iv)). To gain fundamental insight into the charge transfer dynamics, we performed COMSOL multiphysics simulations of the spatial potential distribution during contact and separation states (Figure 3b). The simulation results confirm the validity of the device design principles. Figure 3c illustrates the electron transfer model between two frictional materials.[47,48] When atoms are far apart, their electron clouds do not overlap, and electrons remain confined to their own atomic orbitals. Upon contact under external force, the electron clouds overlap, forming an asymmetric double-well potential. This lowers the energy barrier, allowing electrons to transfer between atoms, resulting in contact electrification.

Through precise control of the drawing rate, we successfully fabricated three types of nanocomposite yarns with distinct diameters and systematically investigated their diameter-dependent triboelectric output performance. As shown in Figure 3d and Figure S5 (Supporting Information), with decreasing drawing rate (corresponding to increasing yarn diameter), the open-circuit voltage (V_{oc}) increases from 14.82 to 22.16 V, the short-circuit current (I_{sc}) rises from 44.75 to 63.45 nA, and the short-circuit transferred charge (Q_{sc}) improves significantly from 4.65 to 6.77 nC. This enhancement phenomenon primarily originates from the reduced surface curvature radius in thicker yarns, which effectively enlarges the true contact area between the yarn and contact materials. A comprehensive study was then conducted on how the concentration of $Cs_3Bi_2Cl_9$ affects the TENG's electrical output (Figure 3e–g). The electrical output characteristics of the TENG demonstrate a distinct concentration-dependent trend. With increasing $Cs_3Bi_2Cl_9$ content, the peak values of V_{OC}, I_{SC}, and Q_{SC} initially increase, reaching maxima of 26.86 V, 90.44 nA, and 8.77 nC at the optimal concentration of 0.75 wt.%, followed by a sharply decrease at the higher concentrations. This performance degradation at elevated $Cs_3Bi_2Cl_9$ content primarily stems from the concurrent suppression of polar β-phase formation and deterioration of nanocomposite dielectric properties, both of which critically compromise the TENG's charge generation and retention efficiency. These findings conclusively establish 0.75 wt.% as the optimal $Cs_3Bi_2Cl_9$ concentration for achieving peak triboelectric performance in this system.

To systematically investigate the triboelectric performance of the CNY-SE-TENG, fabric samples were fabricated by weaving CNYs into both plain and twill structures (Figure S6, Supporting Information). In the testing configuration, a 2 × 2 cm fabric sample serving as the tribo-negative material was fixed on

© 2025 Wiley-VCH GmbH

16163028, 0, Downloaded from https://advanced.onlinelibrary.wiley.com/doi/10.1002/adfm.202523166 by Hangzhou Normal University, Wiley Online Library on [20/11/2025]. See the Terms and Conditions (https://onlinelibrary.wiley.com/terms-and-conditions) on Wiley Online Library for rules of use; OA articles are governed by the applicable Creative Commons License

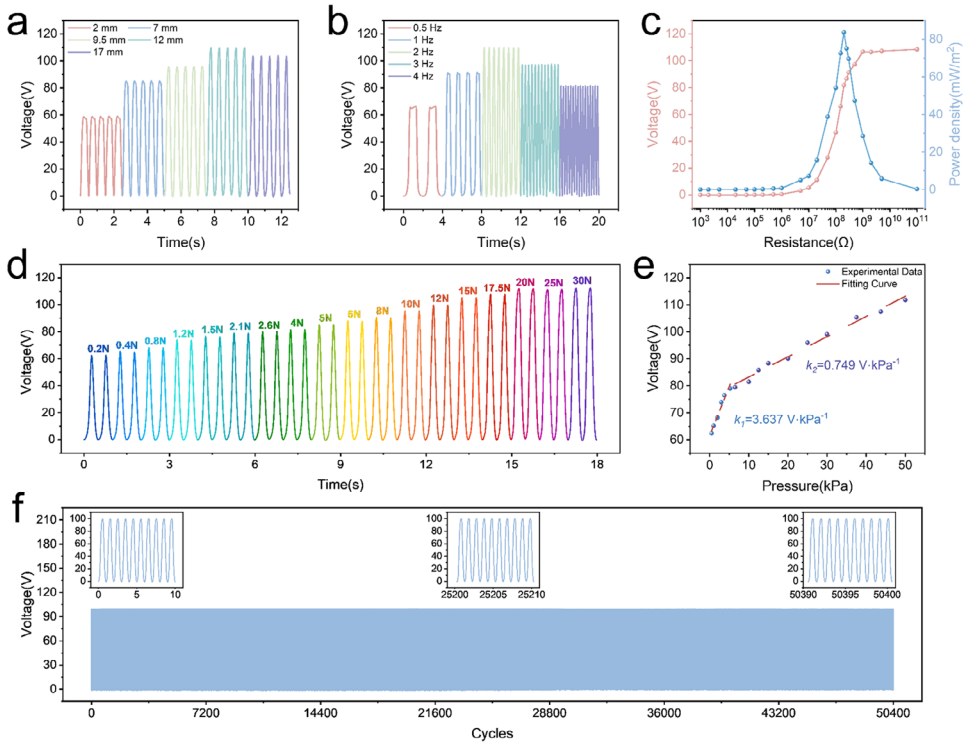

Figure 4. a) Output voltage of the TF-SE-TENG with different displacement distances. b) Output voltage of the TF-SE-TENG at different frequencies. c) Dependence of output voltage and instantaneous power density of the TF-SE-TENG on different load resistances. d) Output voltage of the TF-SE-TENG under different applied force. e) The output voltage of the TF-SE-TENG as a function of the applied pressure. f) The cyclic stability of the TF-SE-TENG over 50 400 cycles.

an acrylic substrate at the terminus of a linear motor, while the counterpart tribo-positive material (another acrylic plate) was mounted on the moving stage of the motor, enabling periodic contact-separation motions at controlled frequency. Comparative tests (Figure S7, Supporting Information) revealed that the TENG based on the twill-structured fabric (TF-SE-TENG) exhibited significantly higher V_{OC} output compared to the plain-woven counterpart, attributing to the enhanced effective contact area resulting from the greater surface roughness of the twill fabric.[49] Consequently, all subsequent triboelectric performance evaluations employed the TF-SE-TENG.

A comprehensive performance evaluation of the optimized TF-SE-TENG was conducted through systematic characterization of its output under varying displacement distances and driving frequencies (**Figure** 4a,b; Figures S8 and S9, Supporting Information). The electrical outputs (V_{OC}, I_{SC}, and Q_{SC}) demonstrated characteristic rise-and-fall profiles, peaking at 9.5 mm displacement and 2 Hz driving frequency. To assess the power density of the TF-SE-TENG, V_{OC} values of the sensor with different external load resistances were recorded in Figure 4c. The V_{OC} value increased with increasing load resistance values, while the power density followed a characteristic unimodal distribution peaking at the matched impedance. The power density was calculated using Equation (2):

$$P = \frac{U^2}{(R \cdot S)} \quad (2)$$

where U represents the instantaneous output voltage, R is the external load resistance, and S denotes the effective contact area. TF-SE-TENG reached its maximum power density of 83.7 mW m^{-2} at a load resistance of 200 MΩ under optimized operating conditions (20 N applied pressure, 9.5 mm displacement, 2 Hz frequency), with measurements performed at 25 °C and 15% relative humidity (RH).

Pressure-dependent measurements revealed a correlation between output voltage and applied force (0.2–20 N range), with signal saturation observed beyond 20 N as the contact area between triboelectric layers reached maximum coverage (Figure 4d). Quantitative sensitivity analysis through pressure-voltage conversion yielded two distinct regimes: a high-sensitivity region (3.637 V kPa^{-1} at 0.2–5.2 kPa) and a reduced-sensitivity region (0.749 V kPa^{-1} above 5.2 kPa) (Figure 4e). Remarkably, the device maintained stable electrical output through 50 400 contact-separation cycles (7 h at 2 Hz, Figure 4f), confirming exceptional operational stability and durability.

Figure 5a compares the power density and durability of our TF-SE-TENG with existing fabric-based TENGs, demonstrating significantly superior to most reported systems.[8,14,24,45,50–55] Crucially, when stored at 20–25 °C, 60%–70% RH, and in dark conditions, the TENG maintained stable electrical output throughout a four-month continuous operation test (Figure 5b), indicating exceptional cycling stability and long-term reliability for wearable energy applications. To evaluate mechanical energy harvesting capability, a 4 cm^2 TF-SE-TENG connected to a rectifier bridge achieved AC-DC conversion, successfully powering 100 LEDs

© 2025 Wiley-VCH GmbH

16163028, 0, Downloaded from https://advanced.onlinelibrary.wiley.com/doi/10.1002/adfm.202523166 by Hangzhou Normal University, Wiley Online Library on [20/11/2025]. See the Terms and Conditions (https://onlinelibrary.wiley.com/terms-and-conditions) on Wiley Online Library for rules of use; OA articles are governed by the applicable Creative Commons License

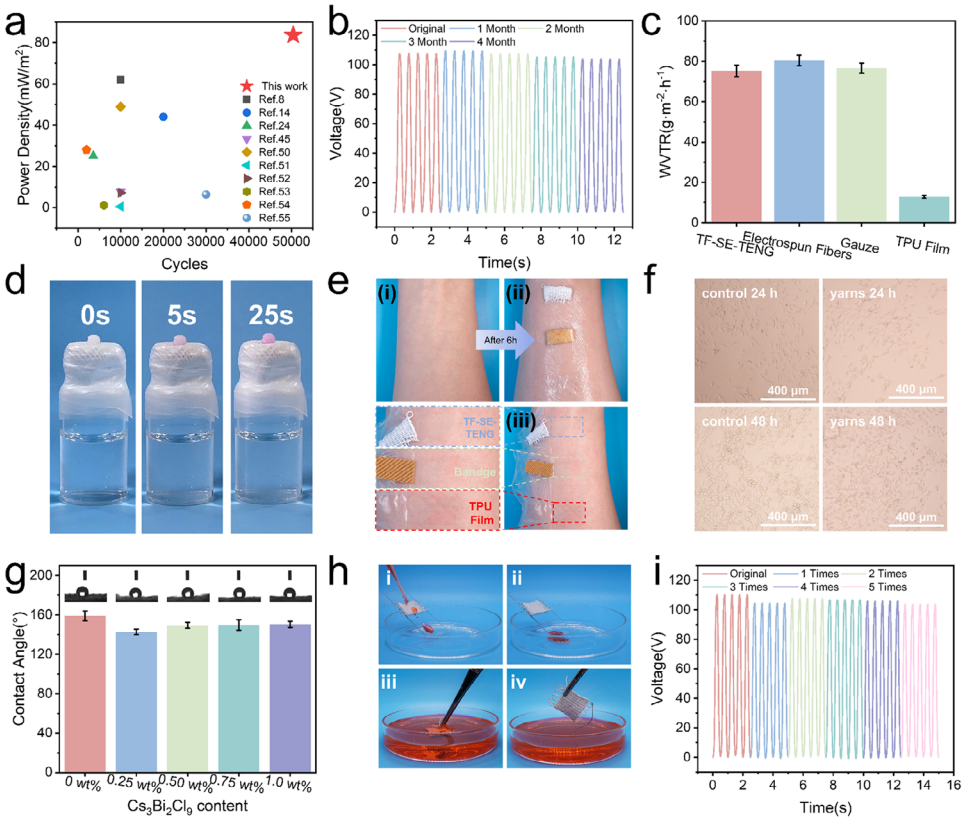

Figure 5. a) Comparison of power density and durability with reported yarn-based TENGs. b) Output stability of the TF-SE-TENG after 4-month storage. c) Comparisons of water vapor transmittance rate of the TF-SE-TENG with other textiles. d) Digital image illustrating the breathability of the TF-SE-TENG. e) Comparison of skin irritation among the TF-SE-TENG, bandage and TPU film. f) The optical microscopy images showing the growth of B16 cells cultured for different durations in both the control group and the experimental group. g) Water contact angle of the TF-SE-TENG with different $Cs_3Bi_2Cl_9$ incorporation levels. h) Photographs of the procedures for drizzling (upper panel) and dipping (lower panel) the TF-SE-TENG with red-dyed water. i) The output voltage of the TF-SE-TENG after 5 washing cycles.

under 20 N cyclic pressure at 2 Hz (Figure S10a and Video S1, Supporting Information). Capacitor charging tests further confirmed efficient energy conversion, with the device charging a 1 μF capacitor to 2.12 V in 40 s (equivalent circuit in Figure S10b, results in Figure S10c, Supporting Information) while a pre-charged 10 μF capacitor powered a hygrometer sensor (Figure S10d and Video S2, Supporting Information).

To address critical wearable application requirements, the moisture permeability, breathability, biocompatibility and wash durability of the TF-SE-TENG were systematically evaluated. Moisture permeability was measured according to GB/T 12 704.2-2009 using the upright cup method, where samples sealed water-filled bottles in a 25 °C, 50% RH environment. Water vapor transmission rate (*WVTR*) was calculated using the Equation (3):

$$\mathrm{WVTR} = \frac{\Delta m}{(A \cdot t)} \tag{3}$$

where Δm denotes water mass loss, A represents effective test area, and t indicates test duration. The *WVTR* range of 66.18–75.54 g m^{-2} h^{-1} observed for the TF-SE-TENGs with different $Cs_3Bi_2Cl_9$ concentrations (Figure 5c; Figure S11, Supporting Information) showed parity with medical bandages and substantially exceeding the 12.77 g m^{-2} h^{-1} of solid TPU membranes. Breathability validation was performed using an ammonia-phenolphthalein assay, where ammonia permeation induced a white-to-purple color transition in cotton balls within 5 s (Figure 5d; Video S3, Supporting Information), visually confirming gas permeability. Biocompatibility assessment involved 6 h epidermal patch testing, which revealed erythema development beneath TPU films and bandages but no skin irritation upon exposure to TF-SE-TENG (Figure 5e). B16 cell co-culture studies demonstrated normal morphology and proliferation after 24- and 48 h exposure (Figure 5f), confirming biosafety. Standard antibacterial testing revealed that the TENG significantly reduced the viability of both Staphylococcus aureus and Escherichia coli relative to the control (Figure S12, Supporting Information), indicating effective activity against Gram-positive and Gram-negative bacteria.

The TF-SE-TENGs with varying $Cs_3Bi_2Cl_9$ concentrations exhibit robust hydrophobicity (contact angles: 142°–150°) (Figure 5g), resulting from the inherent hydrophobicity of PVDF-TrFE combined with electrospun structural features. Droplet tests revealed rapid shedding of red water droplets from tilted surfaces (Figure 5h, upper) and stain resistance after dye

© 2025 Wiley-VCH GmbH

16163028, 0, Downloaded from https://advanced.onlinelibrary.wiley.com/doi/10.1002/adfm.202523166 by Hangzhou Normal University, Wiley Online Library on [20/11/2025]. See the Terms and Conditions (https://onlinelibrary.wiley.com/terms-and-conditions) on Wiley Online Library for rules of use; OA articles are governed by the applicable Creative Commons License

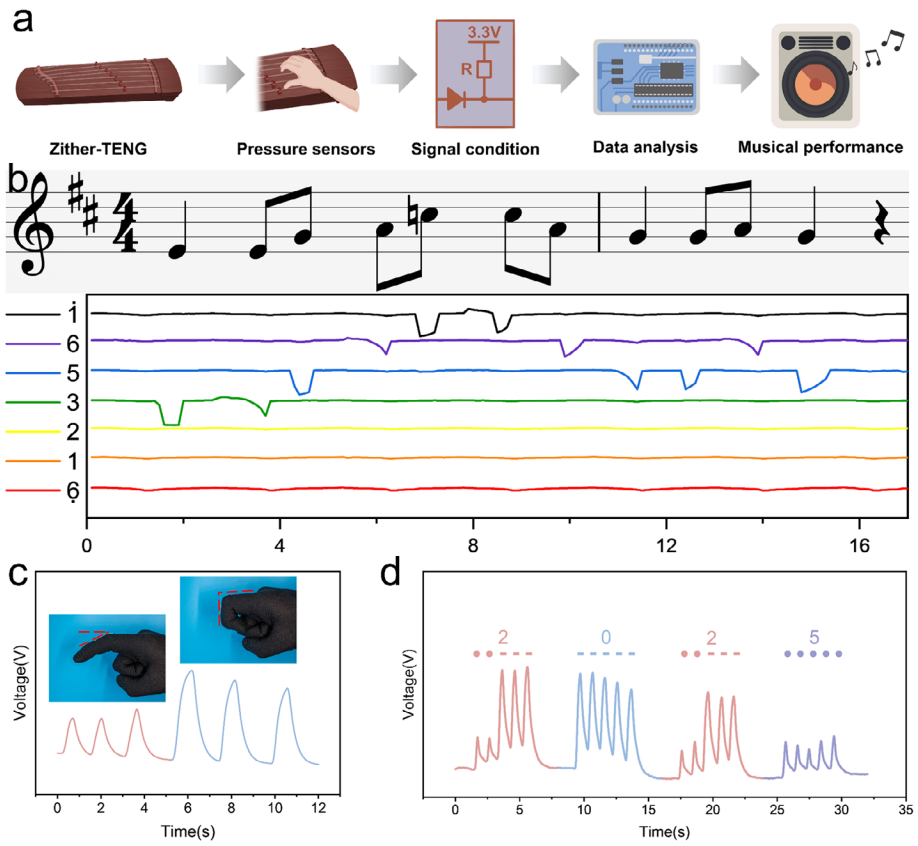

Figure 6. a) Schematic diagram of the workflow of the intelligent Guzheng system. b) Output signals of the intelligent Guzheng system while playing the melody Jasmine Flower. c) Schematic diagram of the Morse code transmission system with an CNY-SE-TENG integrated on glove knuckles. d) Output voltage signals from the CNY-SE-TENG mounted on knuckles, encoding the numeric sequence "2025".

immersion (Figure 5h, lower), verifying non-wetting characteristics. Furthermore, wash durability testing involved 40 min aqueous agitation cycles. After five such cycles, triboelectric output showed negligible attenuation (Figure 5i), validating environmental stability for wearable deployment.

2.3. Application in Interactive Music Interfaces and Communication Recognition

To validate the potential application of the CNY-SE-TENG in developing interactive music interfaces for traditional Chinese instruments, an intelligent Guzheng system was constructed based on an CNY-SE-TENG array. In this system, the traditional strings of the Guzheng were replaced with CNY-SE-TENGs, enabling them to simultaneously collect and output signals during performance. As shown in **Figure 6a**, the TENGs detected mechanical contact from the performer's fingers during plucking and converted the mechanical energy into voltage signals. A real-time signal processing system acquired these electrical signals, translated them into control commands, and drove the audio system to produce corresponding notes, enabling electronic melody performance. This signal transmission relied on the ESP32 microcontroller-based circuit (Figure S13, Supporting Information), which incorporated a multi-channel diode-resistor structure for simultaneous reading of multiple TENG strings. The system demonstrated stable signal acquisition and processing capabilities. When sequentially plucking the seven TENG strings, it accurately played the pentatonic scale melody "6̣, 1, 2, 3, 5, 6, 1⁻,1⁻, 6, 5, 3, 2, 1, 6̣" (Figure S14 and Video S4, Supporting Information). Furthermore, as shown in Figure 6b and Video S5 (Supporting Information), the system correctly reproduced the "Jasmine Flower" melody for the input sequence ″3, 3, 5, 6, 1⁻, 1⁻,6, 5, 5, 6, 5″ with proper note durations. These results verified that the CNY-SE-TENGs combined with the processing system could effectively realize music playback, demonstrating feasibility for constructing intelligent musical instruments and interactive music systems.

To expand the applicability of the CNY-SE-TENG in human-computer interaction and communication recognition, the devices were integrated onto glove knuckles. This system leverages the voltage signals generated by finger bending, utilizing the amplitude differences in voltage pulses caused by varying bending angles to achieve intuitive Morse code encoding (Figure 6c). Specifically, bends below 30° produced low-amplitude pulses, defined as Morse code dots ".", while 90° bends generated high-amplitude pulses, defined as dashes "-". As shown in Figure S15 (Supporting Information), Morse code input for the ten Arabic numerals (0–9) was successfully decoded through temporal control of finger movements and pulse amplitude recognition. For

© 2025 Wiley-VCH GmbH

16163028, 0, Downloaded from https://advanced.onlinelibrary.wiley.com/doi/10.1002/adfm.202523166 by Hangzhou Normal University, Wiley Online Library on [20/11/2025]. See the Terms and Conditions (https://onlinelibrary.wiley.com/terms-and-conditions) on Wiley Online Library for rules of use; OA articles are governed by the applicable Creative Commons License

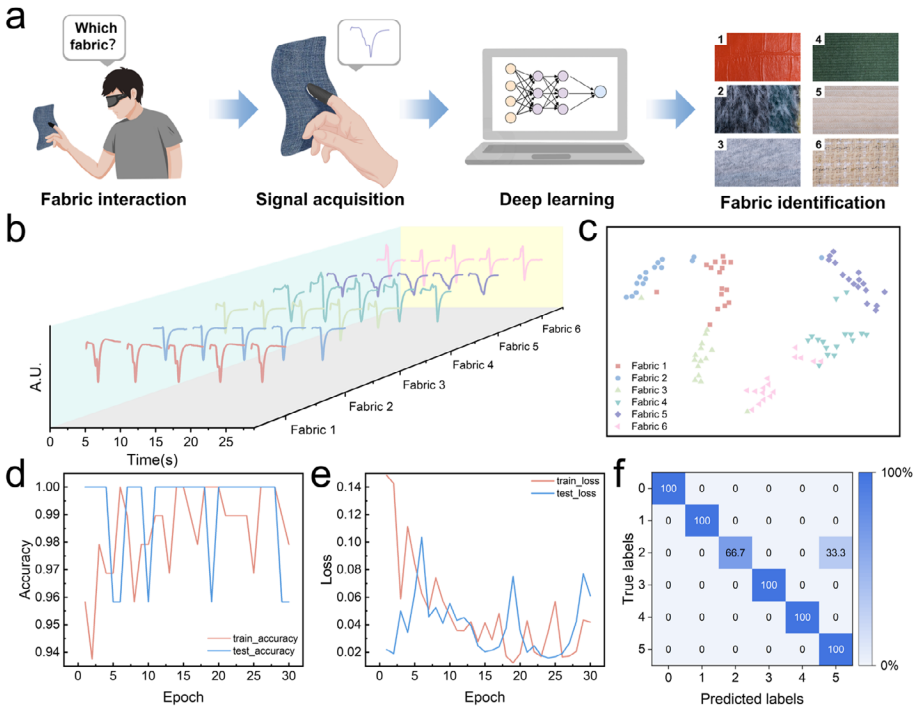

Figure 7. a) Schematic of the workflow of fabric identification. b) The triboelectric signal characteristics of 6 fabrics. c) Visualization of the data set collected from the 6 fabrics. d,e) Training and testing accuracy (d) and loss (e) over training epochs. f) Confusion matrix for the classification of 6 fabrics.

instance, to encode the number "2025" in Figure 6d, the operator sequentially performed finger bends for the digits "2", "0", "2", and "5".

2.4. Application in Recognizing Fabric Patterns

In research on fabric texture perception using TENGs, 2D-structured TENGs face challenges in recognizing fabric patterns due to their contact-mode limitations in extracting micro-surface morphological features. In contrast, 1D-structured TENGs demonstrate significant advantages: When sliding over textured fabrics with concave-convex surfaces, they excite millimeter-scale periodic vibrational contact-separation effects. This unique mechanism not only generates voltage signals containing temporal information but also simultaneously captures mechanical response characteristics induced by micro-topographical variations in fabrics, thereby exhibiting higher sensitivity to subtle texture differences. To validate the fabric texture recognition performance of 1D TENGs, the CNY-SE-TENG was integrated onto the volar surface of the index finger (a critical tactile perception area) of volunteer-worn gloves. Six fabric types with distinct texture characteristics were tested. As shown in **Figure** 7a, the recognition workflow leveraged fabric-specific voltage waveforms generated during sliding contact. These waveforms exhibited high specificity in temporal-mechanical features (e.g., the temporal order of positive and negative signal peaks, oscillation frequency, and peak shape; Figure 7b). This originates from two complementary mechanisms: first, the material's electron affinity determines the temporal order of positive and negative peaks. Second, the contact-separation dynamics, governed by the fabric's stiffness and morphology, define the temporal profile, including oscillation frequency and peak shape. Thus, the combination of peak sequence and waveform morphology provides high identification specificity.

To leverage these characteristic features, a 1D Convolutional Neural Network (1D-CNN) was developed and trained for temporal/mechanical feature analysis. 20 voltage signal samples per fabric type were collected, establishing a standardized dataset of 120 samples across six texture categories (Figure 7c). The dataset was randomly split into training (80%, 96 samples) and testing sets (20%, 24 samples). The network architecture included input, convolutional, pooling, fully-connected, and output layers (detailed in Figure S16, Supporting Information). As shown in Figure 7d,e, the training set loss value decreased continuously and converged rapidly with increasing training epochs, while the test set loss maintained consistently low values (0.08–0.12) despite minor fluctuations. By the 30th epoch, the test set accuracy reached 95.83%. The confusion matrix (Figure 7f) further confirmed the model's high-precision recognition capability across all texture types. This approach not only validates the fabric texture sensing potential of CNY-TENGs but also provides new insights for triboelectric signal-based surface morphology recognition in textiles.

3. Conclusion

This work developed a high-performance CNY-SE-TENG through a scalable one-step electrospinning process incorporating multiscale structure engineering. The engineered core-shell

© 2025 Wiley-VCH GmbH

16163028, 0, Downloaded from https://advanced.onlinelibrary.wiley.com/doi/10.1002/adfm.202523166 by Hangzhou Normal University, Wiley Online Library on [20/11/2025]. See the Terms and Conditions (https://onlinelibrary.wiley.com/terms-and-conditions) on Wiley Online Library for rules of use; OA articles are governed by the applicable Creative Commons License

architecture, comprising a conductive silver-nylon core and PVDF-TrFE/$Cs_3Bi_2Cl_9$ perovskite composite shell, demonstrated significantly enhanced triboelectric output performance. This improvement resulted from the simultaneous optimization of β-phase crystallinity and dielectric properties achieved through strategic $Cs_3Bi_2Cl_9$ incorporation. The CNY-SE-TENG enabled multifunctional applications including interactive musical interfaces for traditional instrument digitization, machine learning-driven textile classification (achieving 95.83% accuracy via 1D-CNN), and self-powered Morse-encoded communication systems. When woven into textiles, it exhibited exceptional pressure sensitivity (3.64 V kPa^{-1}), broad detection range (up to 50 kPa), extreme durability (>50 000 cycles), alongside inherent breathability, biocompatibility and industrial washability. These attributes established the CNY-SE-TENG as a versatile high-performance triboelectric platform for wearable electronics.

4. Experimental Section

Materials: PVDF-TrFE powders (average M_w=5 × 10^5 g/mol) were purchased from Beijing HWRK Chem Co., Ltd. Bismuth oxide (Bi_2O_3, 99%) and Cesium chloride (CsCl, 99.9%) were purchased from Shanghai Aladdin Biochemical Technology Co. Ltd. Hydrochloric acid (HCl, 37 wt.% aqueous solution), *N,N*-dimethylformamide (DMF) and isopropyl alcohol (IPA) of analytical reagent grade were procured from Sinopharm Chemical Reagent Co., Ltd. Acetone (AC) was bought from Huzhou Shuanglin chemical technology Co., Ltd. The core yarns, consisting of 400-denier conductive silver-plated nylon yarn (designated as Ag/Nylon) was commercially sourced from Dongguan Shengxin Special Rope Webbing Co., Ltd. All the materials were used in their as-received state without additional purification.

Synthesis of $Cs_3Bi_2Cl_9$ Perovskites: A precursor solution was synthesized by dissolving 1 mmol of Bi_2O_3 and 3 mmol of CsCl separately in 8 mL of HCl (37 wt.% aqueous solution) under constant magnetic stirring at 100 °C until complete dissolution. The resultant solutions were then stoichiometrically combined and maintained at 100 °C with vigorous stirring for 30 min to ensure homogeneous mixing. The hot precursor solution was subsequently quenched by rapid injection into 60 mL of ice-chilled IPA (4 °C), inducing instantaneous precipitation of white crystalline particles. The colloidal product was isolated through three cycles of centrifugation at 5000 rpm for 10 min with IPA washing, followed by vacuum drying at 70 °C for 10 h to remove residual solvents.

Fabrication of CNY-SE-TENGs: $Cs_3Bi_2Cl_9$ powders (0–30 mg) were initially dispersed in a DMF/AC mixed solvent (7:3 mass ratio) via ultrasonication for 30 min. Subsequently, 3 g of PVDF-TrFE powders were introduced into the dispersion under continuous magnetic stirring at 50 °C for 4 h to achieve a homogeneous PVDF-TrFE/$Cs_3Bi_2Cl_9$ solution with fixed polymer concentration (16 wt.%) and variable $Cs_3Bi_2Cl_9$ loadings (0, 0.25, 0.50, 0.75, and 1.0 wt.% relative to polymer mass). The prepared solution was processed using a dual-syringe configuration (10 mL plastic syringes with 23-gauge needles) coupled to a bipolar high-voltage power supply. The needle-to-collector distance was fixed at 12 cm, with the applied positive and negative voltages set to ±8.0 kV. The feed rate of the PVDF-TrFE/$Cs_3Bi_2Cl_9$ solution was 1.0 mL h^{-1}. The metal trumpet-shaped collector (d= 6.5 cm) was operated at rotational speeds of 300 rpm. The take-up roller (d = 4 cm) was operated at three discrete speeds: 1.5, 3.0, and 4.5 rpm. The nanofiber deposition process was conducted under controlled ambient conditions (25 °C, 60% RH), with continuous environmental monitoring to ensure process stability. The CNY-SE-TENG was constructed using conductive silver-plated nylon yarn as the electrode and a PVDF-TrFE/$Cs_3Bi_2Cl_9$ composite as the triboelectric active layer, operating through single-electrode contact separation mode.

Characterization: The microstructural morphology and elemental composition of PVDF-TrFE/$Cs_3Bi_2Cl_9$ CNYs were characterized using field-emission scanning electron microscopy (FESEM, Supra 55, Zeiss) coupled with energy-dispersive X-ray spectroscopy (EDS). The prepared samples were analyzed by X-ray diffraction (XRD, Dmax2550) and Fourier-transform infrared spectroscopy (FTIR, NICOLET 5700) in attenuated total reflectance (ATR) mode. X-ray photoelectron spectroscopy (XPS) measurements were conducted using a Nexsa G2 spectrometer (ThermoFisher Scientific) with an Al K_α X-ray source (1486.6 eV). The dielectric properties of PVDF-TrFE/$Cs_3Bi_2Cl_9$ nanofiber membranes were investigated using a Novocontrol Alpha-ANB impedance analyzer with frequency sweeps from 10^3 to 10^6 Hz. The inherent self-powered sensing characteristics of the CNY-SE-TENG were evaluated after weaving the CNYs into 2D textile formats. Electrical output from triboelectric effect and pressure-sensing performance of 2D textile-based TENGs were characterized using a custom testing system comprising an electrometer (6514, Keithley), 7.5 Digit Graphical Sampling Multimeter (DMM 7510, Keithley), and a linear motor (B01-37 × 120-c/C1100-GP-XC-0S-000, NTIAG). Open-circuit voltage, short-circuit current and transferred charge were recorded by the electrometer and multimeter, respectively, while the linear motor applied periodic external forces at a fixed frequency. In accordance with the GBT 12 704.2-2009 standard, the moisture permeability of the 2D textile-based TENG was evaluated under controlled conditions (25 °C, 50% RH) using an electronic balance and a temperature and humidity chamber (PCTHI-150T, STIK). The static water contact angles of different samples were measured with a contact angle analyzer (DSA100, KRÜSS). The wearable experiments were conducted with volunteer assistance, with informed consent obtained from all participants prior to measurements.

Statistical Analysis: All quantitative data were presented as mean ± standard deviation (SD). The sample size (n) for each experiment was provided in the corresponding figure legends (typically n = 3–5). No data normalization, transformation or exclusion of outliers was applied. As this study focuses on material preparation, property characterization, and proof-of-concept demonstrations, it employed only descriptive statistics and did not perform any hypothesis testing.

Supporting Information

Supporting Information is available from the Wiley Online Library or from the author.

Acknowledgements

Y.C. and J.H. contributed equally to this work. This work was supported by Natural Science Foundation of Zhejiang Province (Grant Nos. LY23E030002, LRG25E030003) and National Natural Science Foundation of China (Grant Nos. U25A20576, 52273070).

Conflict of Interest

The authors declare no conflict of interest.

Data Availability Statement

The data that support the findings of this study are available from the corresponding author upon reasonable request.

Keywords

nanofibers, PVDF-TrFE, smart fibers, triboelectric nanogenerators, wearable electronics

Received: September 1, 2025
Revised: October 26, 2025
Published online:

© 2025 Wiley-VCH GmbH

16163028, 0, Downloaded from https://advanced.onlinelibrary.wiley.com/doi/10.1002/adfm.202523166 by Hangzhou Normal University, Wiley Online Library on [20/11/2025]. See the Terms and Conditions (https://onlinelibrary.wiley.com/terms-and-conditions) on Wiley Online Library for rules of use; OA articles are governed by the applicable Creative Commons License

[1] W.-G. Kim, D.-W. Kim, I.-W. Tcho, J.-K. Kim, M.-S. Kim, Y.-K. Choi, *ACS Nano* **2021**, *15*, 258.
[2] Y. Yang, X. Guo, M. Zhu, Z. Sun, Z. Zhang, T. He, C. Lee, *Adv. Energy Mater.* **2023**, *13*, 2203040.
[3] X. Zhao, Z. Sun, C. Lee, *Adv. Funct. Mater.* **2024**, *34*, 2409558.
[4] Z. Lai, J. Xu, C. R. Bowen, S. Zhou, *Joule* **2022**, *6*, 1501.
[5] Y. Mao, Y. Li, J. Xie, H. Liu, C. Guo, W. Hu, *Nano Energy* **2021**, *84*, 105918.
[6] C. Dong, A. Leber, D. Yan, H. Banerjee, S. Laperrousaz, T. D. Gupta, S. Shadman, P. M. Reis, F. Sorin, *Sci. Adv.* **2022**, *8*, abo0869.
[7] S. Lin, W. Yang, X. Zhu, Y. Lan, K. Li, Q. Zhang, Y. Li, C. Hou, H. Wang, *Nat. Commun.* **2024**, *15*, 2374.
[8] Y. Wang, L. Chu, S. Meng, M. Yang, Y. Yu, X. Deng, C. Qi, T. Kong, Z. Liu, *Adv. Sci.* **2024**, *11*, 2401436.
[9] X. Peng, K. Dong, C. Ye, Y. Jiang, S. Zhai, R. Cheng, D. Liu, X. Gao, J. Wang, Z. L. Wang, *Sci. Adv.* **2020**, *6*, aba9624.
[10] T. Ahmed, Y. Gao, M. Y. So, D. Tan, J. Lu, J. Zhang, Q. Wang, X. Liu, B. Xu, *Adv. Funct. Mater.* **2024**, *34*, 2408680.
[11] A. Yu, Y. Zhu, W. Wang, J. Zhai, *Adv. Funct. Mater.* **2019**, *29*, 1900098.
[12] S. M. Purushothaman, M. F. Tronco, B. Kottathodi, I. Royaud, M. Ponçot, N. Kalarikkal, S. Thomas, D. Rouxel, *Polymer* **2023**, *283*, 126179.
[13] L. Lu, J. Wu, Y. Zhang, C. Liu, Y. Hu, B. Chen, Y. Zhu, Y. Mao, *Nano Res.* **2025**, *18*, 94907924.
[14] C. Ye, S. Yang, J. Ren, S. Dong, L. Cao, Y. Pei, S. Ling, *ACS Nano* **2022**, *16*, 4415.
[15] P. Manchi, M. V. Paranjape, S. A. Graham, A. Kurakula, J. K. Lee, V. S. Kavarthapu, J. S. Yu, *Adv. Funct. Mater.* **2024**, *34*, 2400371.
[16] M. Zhou, F. Xu, L. Ma, Q. Luo, W. Ma, R. Wang, C. Lan, X. Pu, X. Qin, *Nano Energy* **2022**, *104*, 107885.
[17] C. Zhi, S. Shi, S. Zhang, Y. Si, J. Yang, S. Meng, B. Fei, J. Hu, *Nano-Micro Lett.* **2023**, *15*, 60.
[18] D. Wang, D. Zhang, Y. Yang, Q. Mi, J. Zhang, L. Yu, *ACS Nano* **2021**, *15*, 2911.
[19] V. P. Kallupadi, H. Varghese, U. N. S. Hareesh, A. Chandran, *Adv. Funct. Mater.* **2025**, *35*, 2411855.
[20] S. Qiu, X. Teng, Y. Zhang, X. Wang, K. Chen, J. Zhao, Q. Huang, *Chem. Eng. J.* **2025**, *505*, 159501.
[21] P. Yang, Y. Shi, X. Tao, Z. Liu, X. Dong, Z. L. Wang, X. Chen, *Matter* **2023**, *6*, 1295.
[22] B. Zhang, Y. Jiang, T. Ren, B. Chen, R. Zhang, Y. Mao, *Int. J. Extreme Manuf.* **2024**, *6*, 062003.
[23] L. Shi, H. Jin, S. Dong, S. Huang, H. Kuang, H. Xu, J. Chen, W. Xuan, S. Zhang, S. Li, X. Wang, J. Luo, *Nano Energy* **2021**, *80*, 105599.
[24] T. Yang, C. Wan, X. Zhang, T. Liu, L. Niu, J. Fang, Y. Liu, *Nano Res.* **2024**, *17*, 4478.
[25] J.-K. Kim, G. H. Han, S.-W. Kim, H. J. Kim, R. Purbia, D.-M. Lee, J. K. Kim, H. J. Hwang, H.-C. Song, D. Choi, S.-W. Kim, Z. L. Wang, J. M. Baik, *Energy Environ. Sci.* **2023**, *16*, 598.
[26] X. Luo, L. Zhu, Y.-C. Wang, J. Li, J. Nie, Z. L. Wang, *Adv. Funct. Mater.* **2021**, *31*, 2104928.
[27] C. Zhi, S. Zhang, H. Wu, Y. Ming, S. Shi, W.-F. Io, S. Meng, Y. Si, B. Fei, J. Hao, J. Hu, *ACS Nano* **2024**, *18*, 9365.
[28] F. Jiang, X. Zhou, J. Lv, J. Chen, J. Chen, H. Kongcharoen, Y. Zhang, P. S. Lee, *Adv. Mater.* **2022**, *34*, 2200042.
[29] V. S. Kavarthapu, S. A. Graham, P. Manchi, M. V. Paranjape, J. S. Yu, *Adv. Fiber Mater.* **2023**, *5*, 1685.
[30] Z. Peng, J. Shi, X. Xiao, Y. Hong, X. Li, W. Zhang, Y. Cheng, Z. Wang, W. J. Li, J. Chen, M. K. H. Leung, Z. Yang, *Nat. Commun.* **2022**, *13*, 7835.
[31] Z. Niu, Q. Wang, J. Lu, Y. Hu, J. Huang, W. Zhao, Y. Liu, Y.-Z. Long, G. Han, *Small* **2024**, *20*, 2307810.
[32] J. Liu, Q. Hu, H. Yu, H. Xu, J. Yu, Q. Han, W. Wu, *Inorg. Chem.* **2023**, *62*, 9111.
[33] H. Derikvand, N. Tahmasebi, S. Barzegar, *J. Phys. Chem. Solids* **2023**, *181*, 111528.
[34] J.-Z. Kong, L.-P. Xu, C.-L. Wang, Y.-X. Jiang, Y.-Q. Cao, F. Zhou, *J. Alloys Compd.* **2017**, *719*, 401.
[35] Q. Zhou, Z. Bai, W.-G. Lu, Y. Wang, B. Zou, H. Zhong, *Adv. Mater.* **2016**, *28*, 9163.
[36] L. Canil, T. Cramer, B. Fraboni, D. Ricciarelli, D. Meggiolaro, A. Singh, M. Liu, M. Rusu, C. M. Wolff, N. Phung, Q. Wang, D. Neher, T. Unold, P. Vivo, A. Gagliardi, F. De Angelis, A. Abate, *Energy Environ. Sci.* **2021**, *14*, 1429.
[37] G. Li, Z. Su, L. Canil, D. Hughes, M. H. Aldamasy, J. Dagar, S. Trofimov, L. Wang, W. Zuo, J. J. Jerónimo-Rendon, M. M. Byranvand, C. Wang, R. Zhu, Z. Zhang, F. Yang, G. Nasti, B. Naydenov, W. C. Tsoi, Z. Li, X. Gao, Z. Wang, Y. Jia, E. Unger, M. Saliba, M. Li, A. Abate, *Science* **2023**, *379*, 399.
[38] Y. Xu, X. Guo, Z. Lin, Q. Wang, J. Su, J. Zhang, Y. Hao, K. Yang, J. Chang, *Angew. Chem., Int. Ed.* **2023**, *62*, 202306229.
[39] Y. Zhao, M. Jia, X. Wang, X. Sun, Z. Li, *Polymer* **2024**, *293*, 126681.
[40] J.-Y. Ren, G. Zhang, Y. Li, J. Lei, L. Zhu, G.-J. Zhong, Z.-M. Li, *Polymer* **2018**, *158*, 204.
[41] H. Liu, Z. Wang, J. Xie, C. Guo, W. Hu, *J. Energy Storage* **2022**, *55*, 105618.
[42] P. Martins, A. C. Lopes, S. Lanceros-Mendez, *Prog. Polym. Sci.* **2014**, *39*, 683.
[43] J. Chen, Z. Pei, B. Chai, P. Jiang, L. Ma, L. Zhu, X. Huang, *Adv. Mater.* **2024**, *36*, 2308670.
[44] L. Zhu, Q. Wang, *Macromolecules* **2012**, *45*, 2937.
[45] W. Akram, Q. Chen, X. Zhang, S. Ren, L. Niu, *J. Fang, Nano Energy* **2024**, *131*, 110275.
[46] L. Ma, M. Zhou, R. Wu, A. Patil, H. Gong, S. Zhu, T. Wang, Y. Zhang, S. Shen, K. Dong, L. Yang, J. Wang, W. Guo, Z. L. Wang, *ACS Nano* **2020**, *14*, 4716.
[47] K. Xiao, W. Wang, K. Wang, H. Zhang, S. Dong, J. Li, *Adv. Funct. Mater.* **2024**, *34*, 2404744.
[48] Z. L. Wang, A. C. Wang, *Mater. Today* **2019**, *30*, 34.
[49] S. Bakhtiyari, R. Bagherzadeh, N. Ezazshahabi, A. Jahanshahi, L. Van Langenhove, B. Malengier, *Adv. Mater. Technol.* **2025**, *10*, 2401346.
[50] K. Chen, Y. Li, G. Yang, S. Hu, Z. Shi, G. Yang, *Adv. Funct. Mater.* **2023**, *33*, 2304809.
[51] C. Wei, R. Cheng, C. Ning, X. Wei, X. Peng, T. Lv, F. Sheng, K. Dong, Z. L. Wang, *Adv. Funct. Mater.* **2023**, *33*, 2303562.
[52] Q. Zhong, Y. Mao, B. Zhou, W. Hu, *Chem. Eng. J.* **2025**, *504*, 158871.
[53] Y. Li, Y. Zhang, J. Yi, X. Peng, R. Cheng, C. Ning, F. Sheng, S. Wang, K. Dong, Z. L. Wang, *EcoMat* **2022**, *4*, 12191.
[54] G. Wu, M. Xu, M. Lei, M. Liao, Y. Luo, Y. OuYang, J. Liu, G. Cai, *Mater. Horiz.* **2025**, *12*, 1246.
[55] X. Wang, X. Guan, Z. He, L. Li, Y. Gao, D. Tan, T. Yin, H. Fu, B. Xu, *Nano Energy* **2025**, *142*, 111287.

© 2025 Wiley-VCH GmbH

16163028, 0, Downloaded from https://advanced.onlinelibrary.wiley.com/doi/10.1002/adfm.202523166 by Hangzhou Normal University, Wiley Online Library on [20/11/2025]. See the Terms and Conditions (https://onlinelibrary.wiley.com/terms-and-conditions) on Wiley Online Library for rules of use; OA articles are governed by the applicable Creative Commons License